remote sensing

MDPI

Article

Large-Kernel Central Block Masked Convolution and Channel Attention-Based Reconstruction Network for Anomaly Detection of High-Resolution Hyperspectral Imagery

Qiong Ran [1], Hong Zhong [1,2], Xu Sun [2,*], Degang Wang [2,3] and He Sun [2]

[1] Faculty of Information Science and Technology, Beijing University of Chemical Technology, Beijing 100029, China; ranqiong@mail.buct.edu.cn (Q.R.); 2022210533@buct.edu.cn (H.Z.)
[2] Key Laboratory of Computational Optical Imaging Technology, Aerospace Information Research Institute, Chinese Academy of Sciences, Beijing 100094, China; wangdegang20@mails.ucas.ac.cn (D.W.); sunhe@aircas.ac.cn (H.S.)
[3] College of Resources and Environment, University of Chinese Academy of Sciences, Beijing 100049, China
* Correspondence: sunxu@aircas.ac.cn

Abstract: In recent years, the rapid advancement of drone technology has led to an increasing use of drones equipped with hyperspectral sensors for ground imaging. Hyperspectral data captured via drones offer significantly higher spatial resolution, but this also introduces more complex background details and larger target scales in high-resolution hyperspectral imagery (HRHSI), posing substantial challenges for hyperspectral anomaly detection (HAD). Mainstream reconstruction-based deep learning methods predominantly emphasize spatial local information in hyperspectral images (HSIs), relying on small spatial neighborhoods for reconstruction. As a result, large anomalous targets and background details are often well reconstructed, leading to poor anomaly detection performance, as these targets are not sufficiently distinguished from the background. To address these limitations, we propose a novel HAD network for HRHSI based on large-kernel central block masked convolution and channel attention, termed LKCMCA. Specifically, we first employ the pixel-shuffle technique to reduce the size of anomalous targets without losing image information. Next, we design a large-kernel central block masked convolution to make the network pay more attention to the surrounding background information, enabling better fusion of the information between adjacent bands. This, coupled with an efficient channel attention mechanism, allows the network to capture deeper spectral features, enhancing the reconstruction of the background while suppressing anomalous targets. Furthermore, we introduce an adaptive loss function by down-weighting anomalous pixels based on the mean absolute error. This loss function is specifically designed to suppress the reconstruction of potentially anomalous pixels during network training, allowing our model to be considered an excellent background reconstruction network. By leveraging reconstruction error, the model effectively highlights anomalous targets. Meanwhile, we produced four benchmark datasets specifically for HAD tasks using existing HRHSI data, addressing the current shortage of HRHSI datasets in the HAD field. Extensive experiments demonstrate that our LKCMCA method achieves superior detection performance, outperforming ten state-of-the-art HAD methods on all datasets.

Keywords: high-resolution hyperspectral image; anomaly detection; deep learning; self-supervised learning

check for updates

Citation: Ran, Q.; Zhong, H.; Sun, X.; Wang, D.; Sun, H. Large-Kernel Central Block Masked Convolution and Channel Attention-Based Reconstruction Network for Anomaly Detection of High-Resolution Hyperspectral Imagery. *Remote Sens.* **2024**, *16*, 4125. https://doi.org/10.3390/rs16224125

Academic Editor: Javier Marcello

Received: 21 September 2024
Revised: 23 October 2024
Accepted: 1 November 2024
Published: 5 November 2024

Copyright: © 2024 by the authors. Licensee MDPI, Basel, Switzerland. This article is an open access article distributed under the terms and conditions of the Creative Commons Attribution (CC BY) license (https://creativecommons.org/licenses/by/4.0/).

1. Introduction

In the field of remote sensing, a hyperspectral image (HSI) is a ground-based image collected by hyperspectral sensors mounted on different space platforms. It can record hundreds of consecutive and subdivided spectral bands, which can be used to identify objects made of different materials with the help of small differences in spectra [1–4]. As one of the most popular tasks in the field of hyperspectral remote sensing, hyperspectral

anomaly detection (HAD) [5–7] is the direct detection of spectral signals that differ significantly from the spectra of the surrounding background features as anomalous targets, without exploiting the a priori knowledge of the spectra [8,9]. This method does not require a priori spectral information about the target but rather determines the anomaly target by calculating the difference between each pixel and the background, and the design of a reasonable background model using the acquired data is crucial for locating the anomaly target. Currently, there are two main categories for the most commonly used methods in the field of HAD, i.e., methods based on traditional machine learning and deep learning.

1.1. Traditional Machine Learning-Based Methods

In the early stage of HAD research, researchers assumed that HSIs conformed to certain statistical distributions, and the background was fitted by the calculation of statistical distributions. The Reed–Xiaoli (RX) [10] anomaly detector, as the first statistically based HAD method, assumes that the background data conform to a multivariate Gaussian distribution through the accurate calculation and comparison of the Mahalanobis distances of each pixel from the background distribution. Thus, the anomalous pixels are identified, and on this basis, researchers have proposed detectors Global RX (GRX) and Local RX (LRX) [11] for background modeling and prediction using global and local information of the image, respectively. Since the actual HSI background distribution is more complex and the use of Gaussian distribution does not fit the background well, researchers went on to propose the Kernel RX (KRX) [12] and Segmentation RX (SRX) [13] algorithms. In addition, Liu et al. [14] proposed the 2S-GLRT method for anomaly detection using a design criterion based on the generalized likelihood ratio test and its two-step improvement, which solved the problem of HAD for multi-pixel targets in HSI. Since then, representation-based methods [15–19] have gradually gained widespread attention, such as the collaborative representation-based CRD [20] detector. Li et al. [21] devised a method to estimate the central pixel using a linear combination of samples around a sliding dual window, which effectively distinguishes anomalous from background pixels. The HSIs have low-rank and sparse properties [22], corresponding to background and anomalous pixels, respectively. Zhang et al. [23] used the Mahalanobis distance to impose low-rank background attributes for inverse background covariance matrix estimation, which simultaneously mitigates the inverse covariance matrix problem, anomalous contamination, and parameter instability of the low-rank sparse matrix decomposition. In addition to the above matrix decomposition-based methods, the low-rank representation can also be used to construct a background dictionary using raw HSIs [24]. Several clustering methods have since emerged for obtaining dictionaries, such as K-Means [25] or Mean-Shift [26].

1.2. Deep Learning-Based Methods

Deep neural networks show great advantages in modeling complex datasets and also have strong enough generalization performance. Compared with traditional methods, the deep learning technique can obtain more data features, and in recent years it has been gradually applied to analyze HSI. There are two main directions for deep learning-based HAD methods: similarity measurement-based models and reconstruction-based models. Similarity measurement-based methods require an accurately labeled classification HSI to build tens of thousands of training sample pairs for network parameter tuning. Li et al. [27] proposed a transfer-based deep convolutional neural network (CNN) framework, where they classified pixels by combining the differences between pixel pairs constructed from the center pixel and its surrounding pixels, which were classified by trained CNNs based on the similarity measurement. Subsequently, Rao et al. [28] proposed a transferable network with a Siamese network architecture for anomaly detection by identifying pixels with large differences from the background through similarity scores and demonstrated excellent detection results in experiments. These methods require the high quality and quantity of labeled training data; however, the difficulty of obtaining a priori information about the

target as well as a large amount of HSI data available for training in practical applications makes them not well suited for practical applications.

In contrast, unsupervised learning (USL) anomaly detection models do not require such a priori information but directly use the entire HSI as training data, which significantly simplifies the data processing. Bati et al. [29] pioneered the introduction of the autoencoder (AE) model into the HAD domain, where due to the small percentage of anomalous pixels and the large percentage of background pixels, the network tends to reconstruct the background, and the anomalies behave as reconstruction errors [30]. In order to further explore the spatial context information in HSI, Fan et al. [31] cleverly incorporated graph regularization techniques into the hidden layer of the AE and constructed the RGAE model. Wang et al. [32] proposed an end-to-end automatic anomaly detection (Auto-AD) method based on a fully convolutional AE, which yielded an excellent performance enhancement. In addition, Wang et al. [33] used parameter-free Mahalanobis distance as a means of screening pure background samples and combined spatial and spectral information to further optimize anomaly detection. Recently, researchers have tried to link image denoising with HAD in practice by applying denoising networks to the HAD task. Ma et al. [34] proposed a new diffusion model for background suppression, in which they innovatively input the original HSI into the denoising network and denoised the background as noise, which led to a great improvement in background suppression. Wang et al. [35–39] applied the blind-spot denoising network to HAD and pioneered the self-supervision paradigm in the HAD task, which makes the whole network reconstruct the abnormal pixels by eliminating the receptive field center pixels during the training, with excellent performance in background suppression. Cheng et al. [40,41] combined the AEs with the low-rank and sparse attributes of HSI to enhance the spatial information utilization by a new local training approach, thus making the network more sensitive to local anomalies. They further proposed a new HAD paradigm [42] for representing a wide range of backgrounds, with satisfactory results.

1.3. Motivation and Contribution

Hyperspectral sensors are usually mounted on satellite and airborne platforms to scan for ground objects, and with the development of UAVs and hyperspectral technology, hyperspectral sensors can be mounted on UAVs to detect ground objects. Compared to airborne and satellite-based platforms, HSIs acquired by UAV platforms with hyperspectral sensors have a higher spatial resolution, which can reach the decimeter or even centimeter level [43–48]. At the same time, due to the improved spatial resolution, the target size of high-resolution hyperspectral images (HRHSIs) is also larger compared to that of low- and medium-resolution HSIs.

Mainstream reconstruction-based deep learning methods for HAD have shown promising results in low to medium spatial resolution images. However, these methods often focus predominantly on local spatial neighborhood information during the reconstruction process. When applied to HRHSIs containing larger-scale anomalous targets, these approaches tend to also reconstruct the anomalous targets, causing them to be insufficiently highlighted and leading to missed detections.

To overcome these limitations, this paper introduces a novel HAD method tailored for HRHSIs based on large-kernel central block masked convolution and channel attention (LKCMCA). The proposed LKCMCA begins by downsampling the image using a pixel-shuffle technique, effectively reducing the size of anomalous targets. Then, the downsampled HRHSI serves as labels to extract surrounding background features, aided by a large-kernel central block masked convolution. Meanwhile, the efficient channel attention (ECA) [49] mechanism is exploited to mine the deeper band features, further enhancing the suppression of anomalous pixel reconstruction. To robustly mitigate the reconstruction of anomalous pixels, we introduce an adaptive loss function that down-weights anomalous pixels, optimizing the training process to ensure the network more effectively reconstructs

background pixels, while anomalous targets are prominently highlighted through reconstruction errors. The main contributions of this paper are as follows:

(1) We propose LKCMCA, a novel HAD model specifically designed for HRHSI, demonstrating superior detection performance compared to existing HAD models designed for standard HSI.

(2) To suppress the reconstruction of anomalous pixels and capture broader neighborhood background information, we leverage a large-kernel central block masked convolution. This encourages the network to prioritize reconstructing background pixels over anomalous ones, enabling more effective anomaly detection.

(3) To extract deep spectral features, our LKCMCA employs the efficient channel attention mechanism, which allows the network to effectively suppress anomalous pixel reconstruction by focusing on neighboring spectral dimensions. It leverages both the sparse presence of anomalous pixels in HRHSI and the distinct spectral differences between the background and anomalous targets.

(4) We designed an adaptive loss function that dynamically adjusts the weights of potential anomalous pixels during training based on the mean absolute error. This strategy further suppresses the reconstruction of anomalies, enhancing the detection capability of the proposed model.

The rest of the paper is organized as follows: Section 2 describes the methodological details. Section 3 describes the dataset and details the experiments, and finally, Section 4 concludes the paper.

2. Methods

This work aims to perform anomaly detection on HRHSI; the main process comprises performing background reconstruction on HRHSI, and the high reconstruction error is the anomaly target. In this study, we propose an HAD method based on large-kernel central block masked convolution and channel attention, as shown in Figure 1, which is divided into two main phases. (1) Training phase: pixel-shuffle downsampling of the raw HRHSI is performed first, and the downsampled image is then fed into the reconstruction network. Finally, the inverse pixel-shuffle downsampling is performed on the output of the network, and the reconstruction loss of the LKCMCA network during training is set to the proposed loss function. (2) Detection phase: this phase involves the same steps as the training phase, where we input the original HRHSI into the trained reconstruction network to obtain the background reconstruction result of the original image, and the residual difference between the reconstruction result and the original image is used as the result of HAD, which is described in detail below.

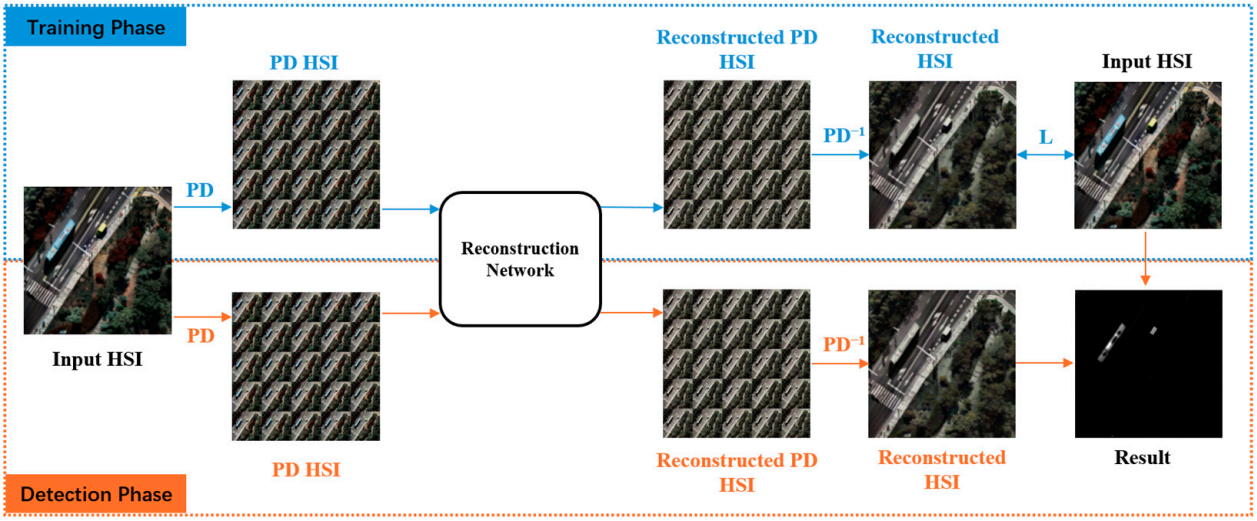


Figure 1. Flowchart of the proposed LKCMCA methodology.

2.1. Training Phase

2.1.1. Pixel-Shuffle Downsampling

Pixel-shuffle downsampling (PD) operations have good applications in blind-spot denoising networks. This operation reduces the spatial correlation between neighboring pixels without the loss of spatial information in the image. The PD operation is shown in the left half of Figure 2. Then, blind-spot networks reconstruct the center pixels using blind-spot convolution. This operation can effectively reduce the correlation between the background pixels and the anomalous pixels, thus suppressing the reconstruction of the anomalous pixels. On the other hand, due to the fixed size of the blind spot, some of the neighboring anomalous pixels will be involved in the reconstruction when facing a larger-scale anomalous target, resulting in the anomalous pixels being reconstructed, which will reduce the detection accuracy. Through the PD operation, large-scale anomalous targets are split and dispersed into various sub-images, ensuring that the anomalous pixels will not be involved in the blind-spot convolution for computation during reconstruction. The last effect of the pixel-shuffle operation is then to expand the receptive field, as shown in the right half of Figure 2. It can be found that when a convolution operation of m $\times$ m is performed on an image with a downsampling factor of n, it is equivalent to performing a dilated convolution of the original image with a dilation rate of n. At the same time, the receptive field will be expanded to (n $\times$ (m $-$ 1) + 1) $\times$ (n $\times$ (m $-$ 1) + 1); this means that the operation can increase the receptive field of the network without changing the structure of the network. Since dilated convolution introduces extra parameters and computational steps into the computer, it results in slower computation speeds than normal convolution in real-world computations. Pixel-shuffle and sampling operations can be used to expand the receptive field without increasing the computation time.

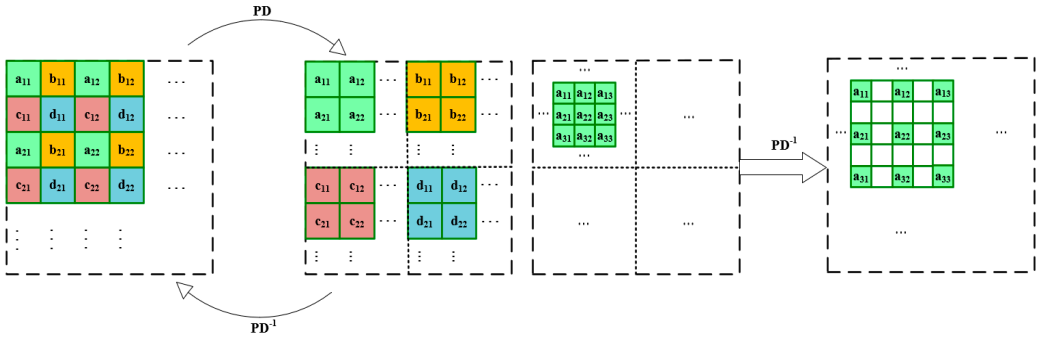


Figure 2. Pixel-shuffle downsampling with a downsampling factor of 2 and the variation of the 3 $\times$ 3 convolution kernel.

2.1.2. Network

The network model is shown in Figure 3, and its basic structure contains three main parts: the blind block feature extraction module, the ECA module, and the residual reconstruction module. The output feature maps have the same spatial size for each layer by setting the padding and step size. PD(X), w_1, and m are the input image after the PD operation, the large-kernel central block masked convolution kernel, and a binary mask of the same size as w_1 and with a central 5 $\times$ 5 region of 0 and the rest of the positions of 1, respectively. The central masked convolution is expressed as

$$f_1 = \mathrm{PD}(X) * (w_1 \odot m), \tag{1}$$

where f_1 denotes the feature map of the first layer, and the symbols $*$ and $\odot$ are the convolution operator and the multiplication of elements, respectively. The second layer is a 3 $\times$ 3 convolutional layer, and the second layer feature map is denoted as

$$f_2 = \mathrm{PD}(X) * (w_1 \odot m) * w_2 = f_1 * w_2, \tag{2}$$

where w_2 denotes a 3 × 3 convolution, f_2 represents the feature map of the second layer (it is worth noting that the first layer of convolution corresponds to a receptive field size of 23 × 23 and a central blind area size of 5 × 5). After the second layer of 3 × 3 convolution, the receptive field size is enlarged to 25 × 25, while the central blind area size is reduced to 3 × 3. The second-layer feature map obtained at this point is a feature map with suppressed anomalous interference and thus can be considered a background feature map that does not contain anomalous pixel information, which is later input into the ECA module.

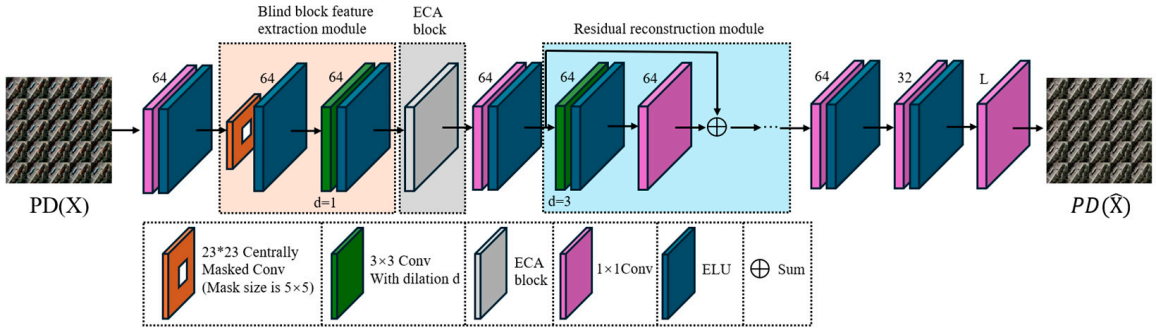


Figure 3. Detailed information of the proposed network structure (the number above Conv, e.g., 64, indicates the number of output channels).

The ECA module is a non-dimensionality-reducing cross-channel interaction strategy, which can adaptively combine the information of neighboring channels to complete cross-channel information interaction. Specifically, the ECA module first adaptively calculates the kernel size of the 1D convolution according to the number of channels. The formula for calculating the kernel size is as follows:

$$k = \left| \frac{\log_2(C)}{\gamma} + \frac{b}{\gamma} \right|_{odd}, \tag{3}$$

where C denotes the number of channels of the input feature image, k is the convolution kernel size, and b and γ are hyperparameters. The output is denoted as

$$f_3 = Conv1D(f_2), \tag{4}$$

where $Conv1D$ denotes a 1D convolution operation and f_3 represents the feature map of the third layer. At this time, the information of each band in the output feature map is a linear combination of the neighboring bands of the same position band of the input feature map. Since the number of anomalous pixels is much lower than the number of background pixels, and the difference in spectral characteristics between anomalous pixels and background pixels is large, the network will tend to reconstruct the background pixels, and the weights of the 1D convolution converge toward the reconstructed background during training. However, because of the significant difference in spectral characteristics between the background and anomalous pixels, the convolution weights of the reconstructed background pixels in the neighboring bands are not able to reconstruct the anomalous pixels when they are applied to the anomalous pixels. This leads to perturbation of the spectral information of the anomalous pixels in the reconstructed bands, thereby inhibiting the reconstruction of the anomalous pixels. At the same time, since the information gap between neighboring bands is small and the size of the convolution kernel is adaptively determined according to the number of channels in the input image, the output feature map avoids the whole image being disrupted due to the introduction of information from bands with large gaps.

Finally, it is fed into a reconstruction module consisting of nine 3 × 3 dilated convolutional residual structures, where the dilation rate is set to 3. After the first layer of dilation convolution, the receptive field covered by a single pixel in the output feature map expands to 31 × 31, while the center portion is covered, that is, each pixel will be

reconstructed using spectral information from the pixel itself, allowing each pixel to be better reconstructed. This can result in the background fitting effect being greatly enhanced, to adapt to the complex background of the HRHSI.

2.1.3. Loss Function

In order to suppress the reconstruction of anomalous pixels, we design an adaptive loss function by down-weighting anomalous pixels based on the mean absolute error. During the training process, the difference between the network output and the original image is expressed as

$$\Delta = y - x, \tag{5}$$

where y is the output image of the network, and x is the input image of the network. The numerical size of the elements in the tensor Δ represents the size of the difference between the pixels at the same location before and after the reconstruction, and the location with the larger value tends to be the location of the anomalous pixels, such that the vector is

$$\Delta_{\max} = (\Delta)_{\max}, \tag{6}$$

where $\Delta_{\max}$ denotes the vector consisting of the maxima of each channel corresponding to each of the tensors in the tensor Δ, which is repeatedly expanded into a tensor consistent with the shape of the original image. Then, the difference with Δ is calculated as

$$W = \Delta_{\max} - \Delta\,. \tag{7}$$

Then, W is normalized to

$$W_n = \frac{W - W_{\min}}{W_{\max} - W_{\min}}, \tag{8}$$

where W_n is the final weight obtained. Then, the loss function is

$$L = L1(y \odot W_n, x \odot W_n), \tag{9}$$

where $L1$ is the mean absolute error loss function, y is the network output result, x is the network input image, and $\odot$ denotes the matrix dot product. We do not adopt the $L2$ loss function given that it is more sensitive to outliers, and it is easier to reconstruct anomalous pixels using the $L2$ loss as compared to the $L1$ loss.

This loss function can adaptively reduce the loss calculation weight of the location of potential abnormal pixels during the training process, which means that the reconstruction of abnormal pixels in the reconstructed result does not greatly affect the decrease of the loss value. The reconstruction of abnormal pixels is suppressed to some extent. On the other hand, due to the introduction of ECA, the information of the anomalous pixels being disrupted will slow down the decline of the loss value to a small extent, and this loss function can avoid this problem well. Although this process also reduces the loss weight of the background pixels at the same time, due to the large difference between the anomalous pixels and the background pixels and the much higher percentage of background pixels, the network will tend to reconstruct the background pixels first. It makes the parts of the network results with large differences from the original image the anomalous pixels.

2.2. Detection Phase

Similarly, in the detection phase, we perform a PD operation using the same down-sampling factors as in training and then feed the sampled image into the trained network R_D parameterized by L. After performing the PD inverse operation, the reconstructed image is calculated as follows:

$$\hat{X} = PD^{-1}(R_D(PD(X); L)). \tag{10}$$

After the above training process, our proposed LKCMCA network is an effective background reconstruction network, which makes the reconstruction result of anomalous pixels similar to the surrounding background. This results in a high reconstruction error for the anomalous target so that the reconstructed HRHSI can be regarded as a background image. Finally, based on the reconstruction error, the anomaly detection results can be obtained using (11), as follows:

$$D_{i,j} = ||x_{i,j} - \hat{x}_{i,j}||_2^2, \tag{11}$$

where $x_{i,j} \in R^{L\times 1}$, $\hat{x}_{i,j} \in R^{L\times 1}$ denote the pixels of X and $\hat{X}$ at position (i, j), respectively, and $D_{i,j}$ denotes the anomaly probability value at the corresponding position; these comprise the final anomaly detection result $D \in R^{R\times C}$.

3. Experimental Results

3.1. Datasets

The datasets used in this study consist of four datasets, the first of which comprises airborne hyperspectral data taken over Rochester Institute of Technology [50] with a spatial resolution of 0.4 m. The anomalous targets are cars, and the equipment used is a Visible Near-Infrared (VNIR) Hyperspectral Headwall Photonics Micro Hyperspec E-Series CMOS sensor manufactured by Headwall, Inc; the band range covers 400 nm to 1000 nm, with 372 bands. The second dataset is the hyperspectral data of visible infrared provided by Guangzhou Xingbo Science Instrument Co., Ltd. (Guangzhou, China), which was taken by a UAV equipped with a spectral imager, model Co-Aligned HP, in which the sensor of VNIR is a CMOS sensor with a spatial resolution of 0.1 m. The scene is an airport runway on which different colors of tarpaulins are placed, and the anomalous targets are these tarpaulins. The band range covers 400 nm to 1000 nm, with 273 bands. The third and fourth datasets are urban scenes captured on Jinshitan Road in Qingdao City, using a UAV with a GaiaSky-mini2-VN hyperspectral camera with a spatial resolution of 0.16m; the anomalous target is a vehicle. The range of bands covers 400 nm to 1000 nm, with a total of 176 bands. The pseudo-color maps of all datasets and their ground truth maps are shown in Figure 4, and the information for these datasets is shown in Table 1.

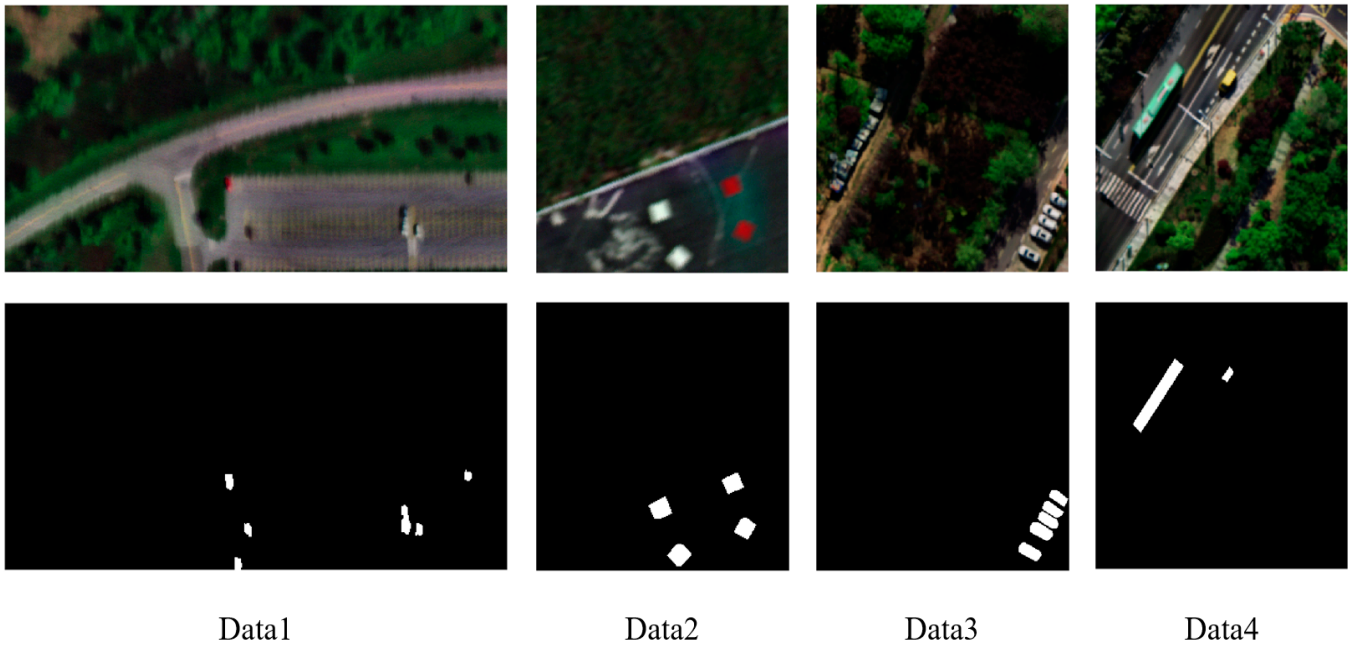


Figure 4. Pseudo-color and ground truth maps for the four datasets.

Table 1. Details of the experimental datasets.

Dataset	Bands	Spatial Size	Resolution
Data1	372	240 × 480	0.4 m
Data2	273	240 × 240	0.1 m
Data3	176	360 × 360	0.16 m
Data4	176	360 × 360	0.16 m

3.2. Comparison Algorithms and Evaluation Metrics

(1) Comparison Algorithms: the comparison algorithms used in the experiments include GRX, LRX, CRDBPSW, FEBPAD, VABS, KIFD, Auto-AD, BSDM, GAED, and RGAE. Among them, GRX and LRX are the traditional detectors, CRDBPSW is the local dual-window-based detector, FEBPAD is the global-based detector, VABS is a visual attention-based detector, KIFD is a kernel isolated forest-based detector, and Auto-AD, BSDM, GAED, and RGAE are the current state-of-the-art deep learning-based architectures.

(2) Evaluation metrics: We adopt the criteria commonly used in the field of HAD to evaluate the detection performance of different methods, i.e., statistical separability plots, receiver operating characteristic (ROC) curves, and the area under the ROC curve (AUC) [51–54]. The ROC curves can show the performance of the model under different thresholds, which can comprehensively reveal the detection effect of the method, and the corresponding AUC values can quantitatively show the accuracy metrics. AUC values can quantitatively show the accuracy index. The better the performance of the detector, the closer its corresponding ROC curve is to the upper left corner, while its AUC value is close to 1. In addition, the separability boxplot demonstrates intuitively the statistical distribution of anomalous response values at the pixel positions of the background and anomaly categories. In this plot, the response values of the background and anomaly categories are grouped in two different colored boxes, where the background category is represented in blue and the anomaly category is presented in red. Each box shows a range of data from 10% to 90%. If the algorithm performs well in suppressing the background and separating the anomalies, then the blue background box will be located lower on the chart and will have a relatively narrow width showing a high concentration of the background response values. At the same time, the red anomaly box will be significantly different in position from the blue box.

3.3. Parameter Setting

The hyperparameters b and γ in the ECA module are set to 1 and 2, respectively. The downsampling factor is set to four for the Data1 dataset and to six for the rest of the datasets in the training process as well as in the test; the number of training epochs is 3000.

3.4. Detection Performance for Different Methods

Figures 5–8 show the maps of anomaly detection results for the 11 detectors on the four datasets, where the first map shows the ground truth of the dataset and the rest show the detection results for the different methods. Figures 9 and 10 show the ROC curves and separability boxplots of these 11 algorithms on the four datasets.

As shown in Figures 5–8, for the real scene dataset, the proposed LKCMCA method produces very satisfactory results in terms of background suppression and anomaly highlighting by comparing with the ground truth. As shown in the Data1 dataset, the proposed method achieves the best results in terms of background suppression, with all anomalous targets detected by KIFD, Auto-AD, and BSDM, but with just as many false alarms. GRX and FEBPAD have better background suppression effects, but both fail to detect all anomalous targets. Our proposed LKCMCA method has a weak response for some of the anomalous targets but detects all of them and also has the best background suppression effect. In addition, the result maps of the Data2 dataset show that CRDBPSW, VABS, KIFD, and Auto-AD can only detect the edges of the anomalous targets and not the interiors of the

anomalous targets, which means that these methods only detect local anomalies and not global anomalies, and they do not apply to HRHSIs. Meanwhile, the detection results of the two groups of anomalous targets are not stable for the methods proposed by FEBPAD, VABS, GAED, and RGAE; the anomalous responses of one group are strong, and the other group is very weak. RAGE is unstable in detecting these two groups of anomalous targets; one group of anomalous response is strong, and the other group of anomalous response is very weak. Our proposed method can detect these two groups of targets well. We can see from the experimental result maps of the Data3 dataset that most of the methods have good background suppression effects on this dataset. However, these methods suppress the anomalous targets while suppressing the background, and the anomalous response is not only very weak but also fails to detect the anomalous targets completely. The KIFD, GAED, and RGAE methods are able to detect anomalous targets well, but they are not as effective as our proposed LKCMCA method in terms of background suppression. The effect is not as good as our LKCMCA method, it can be seen that LKCMCA has the best balance between the detection of anomalous targets and the suppression of backgrounds. Finally, from the experimental results on the Data4 dataset, it can be seen that our proposed LKCMCA method is better than the other methods in terms of background suppression, and it has a good detection effect for the anomalous targets.

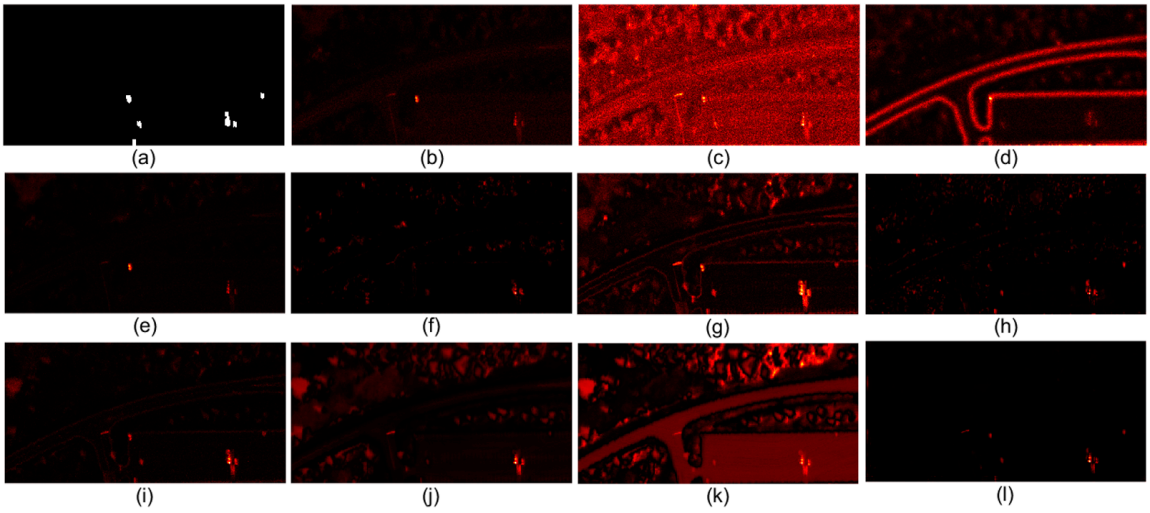


Figure 5. HAD colored maps obtained by different algorithms on the Data1 dataset. (**a**) Ground truth, (**b**) GRX, (**c**) LRX, (**d**) CRDBPSW, (**e**) FEBPAD, (**f**) VABS, (**g**) KIFD, (**h**) Auto-AD, (**i**) BSDM, (**j**) GAED, (**k**) RGAE, and (**l**) LKCMCA.

Indeed, in addition to the visual appearance of the HAD colored maps, other metrics are needed to qualitatively and quantitatively assess the performance of the different algorithms. Figure 9 shows the ROC results of the 11 algorithms on these four datasets. It can be seen that in most cases, the brown curve of the proposed LKCMCA method is higher than the other curves, and the AUC values are higher than the others. Although the AUC values and ROC curves of the BSDM method on the Data3 dataset are slightly higher than those of our LKCMCA, we can see through the HAD colored map in Figure 7 that the anomalous response values of LKCMCA are much higher than those of the BSDM method, and that the BSDM method is not as effective as it should be in the Data4 dataset. Figure 10 demonstrates the background and anomaly separability ability of these 11 algorithms; although the red anomaly box of our LKCMCA does not occupy the highest position, the blue background boxes are all very narrow and distributed in a very small range, which verifies the background suppression performance of our model. Comparing the results in Figure 10c, it can be found that the red box of our LKCMCA is much higher than that of the BSDM method, while the blue box is almost as narrow, which reflects the superiority of LKCMCA in background and anomaly separability.

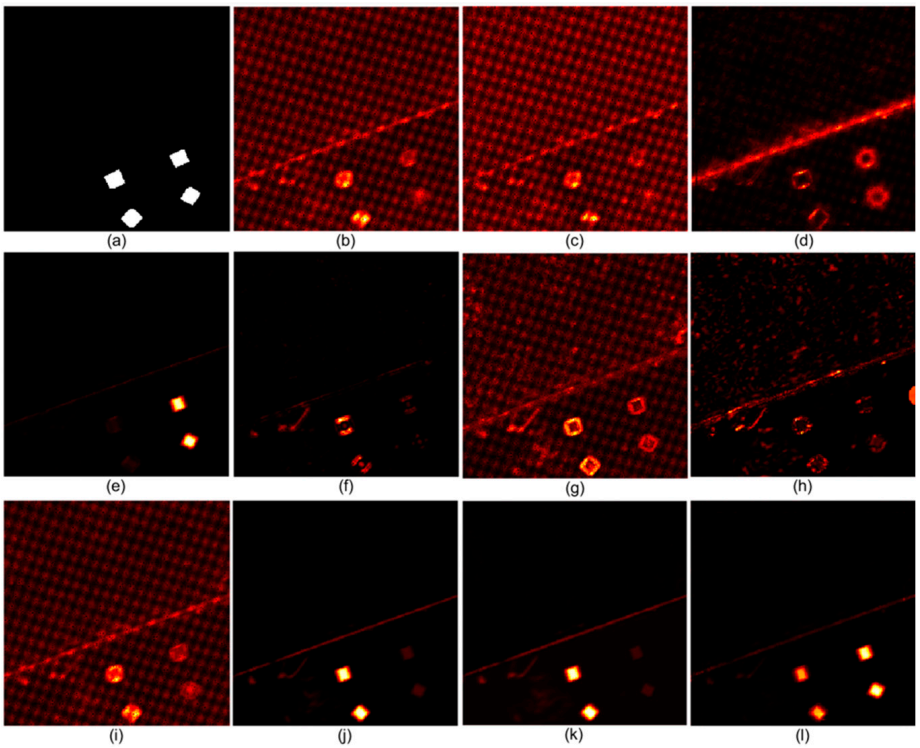


Figure 6. HAD colored maps obtained by different algorithms on the Data2 dataset. (**a**) Ground truth, (**b**) GRX, (**c**) LRX, (**d**) CRDBPSW, (**e**) FEBPAD, (**f**) VABS, (**g**) KIFD, (**h**) Auto-AD, (**i**) BSDM, (**j**) GAED, (**k**) RGAE, and (**l**) LKCMCA.

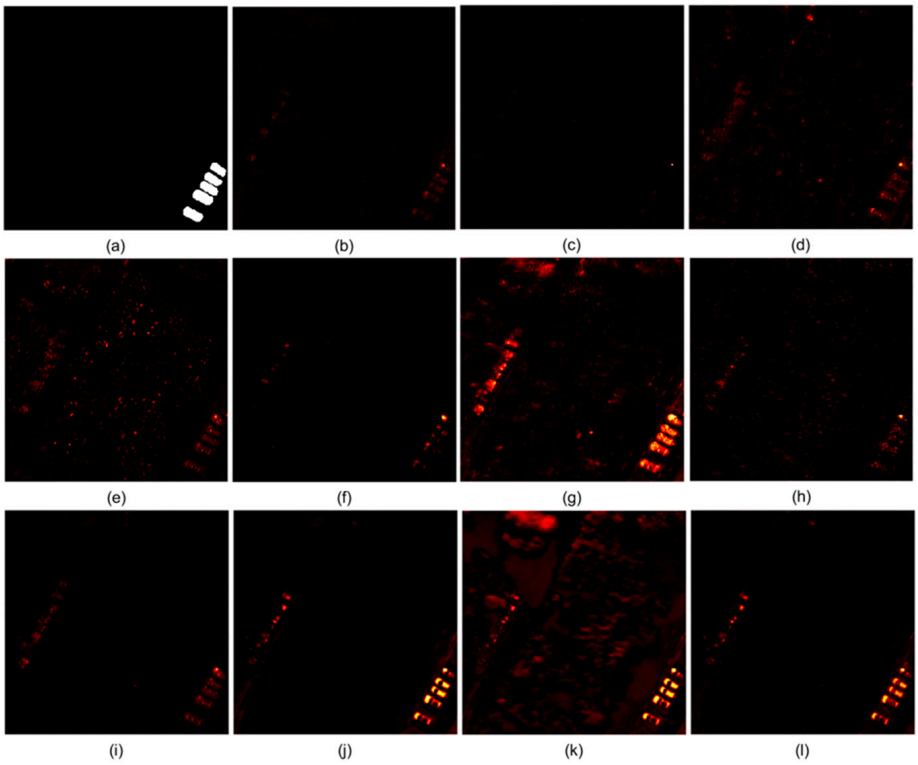


Figure 7. HAD colored maps obtained by different algorithms on the Data3 dataset. (**a**) Ground truth, (**b**) GRX, (**c**) LRX, (**d**) CRDBPSW, (**e**) FEBPAD, (**f**) VABS, (**g**) KIFD, (**h**) Auto-AD, (**i**) BSDM, (**j**) GAED, (**k**) RGAE, and (**l**) LKCMCA.

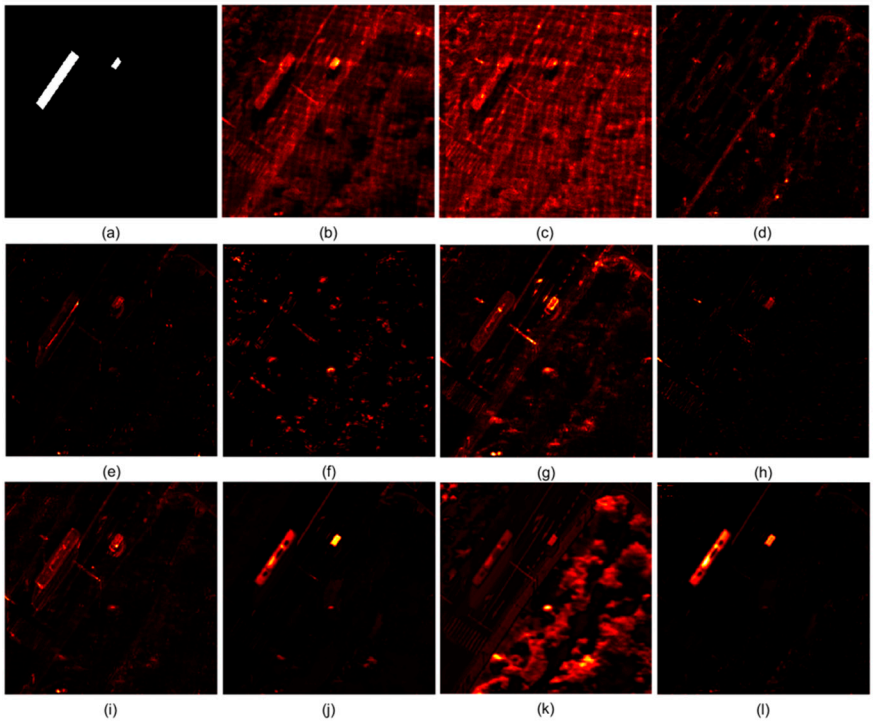


Figure 8. HAD colored maps obtained by different algorithms on the Data4 dataset. (**a**) Ground truth, (**b**) GRX, (**c**) LRX, (**d**) CRDBPSW, (**e**) FEBPAD, (**f**) VABS, (**g**) KIFD, (**h**) Auto-AD, (**i**) BSDM, (**j**) GAED, (**k**) RGAE, and (**l**) LKCMCA.

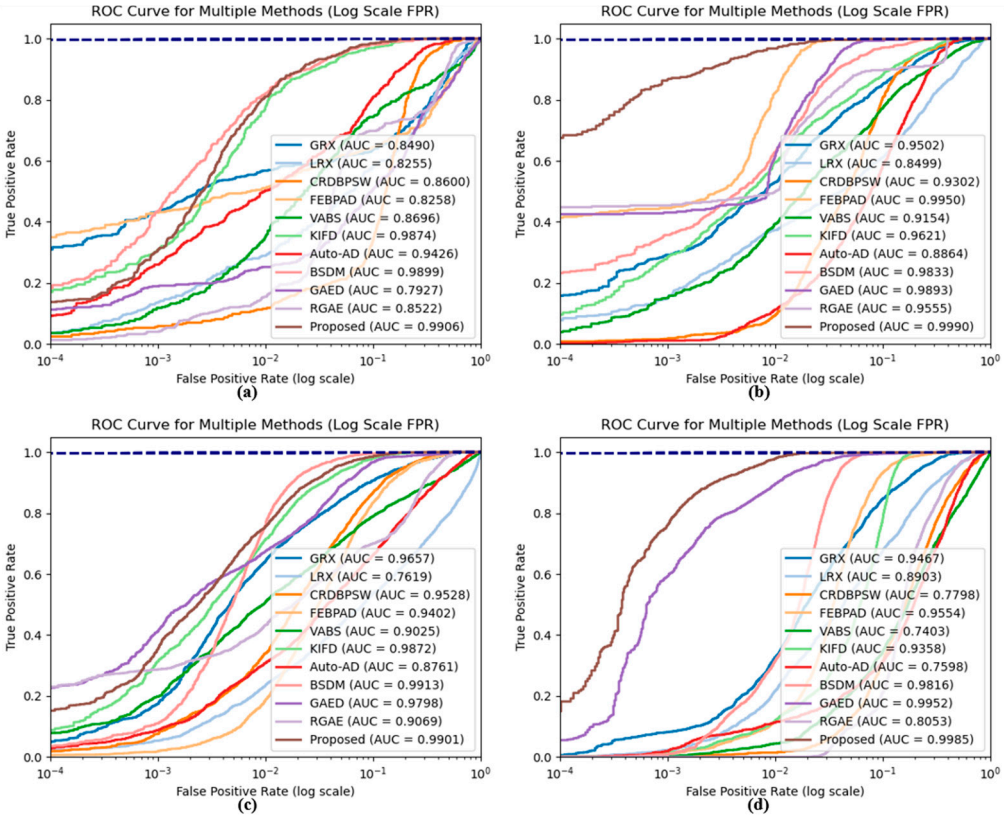


Figure 9. ROC curves of different algorithms on four datasets: (**a**) Data1, (**b**) Data2, (**c**) Data3, and (**d**) Data4.

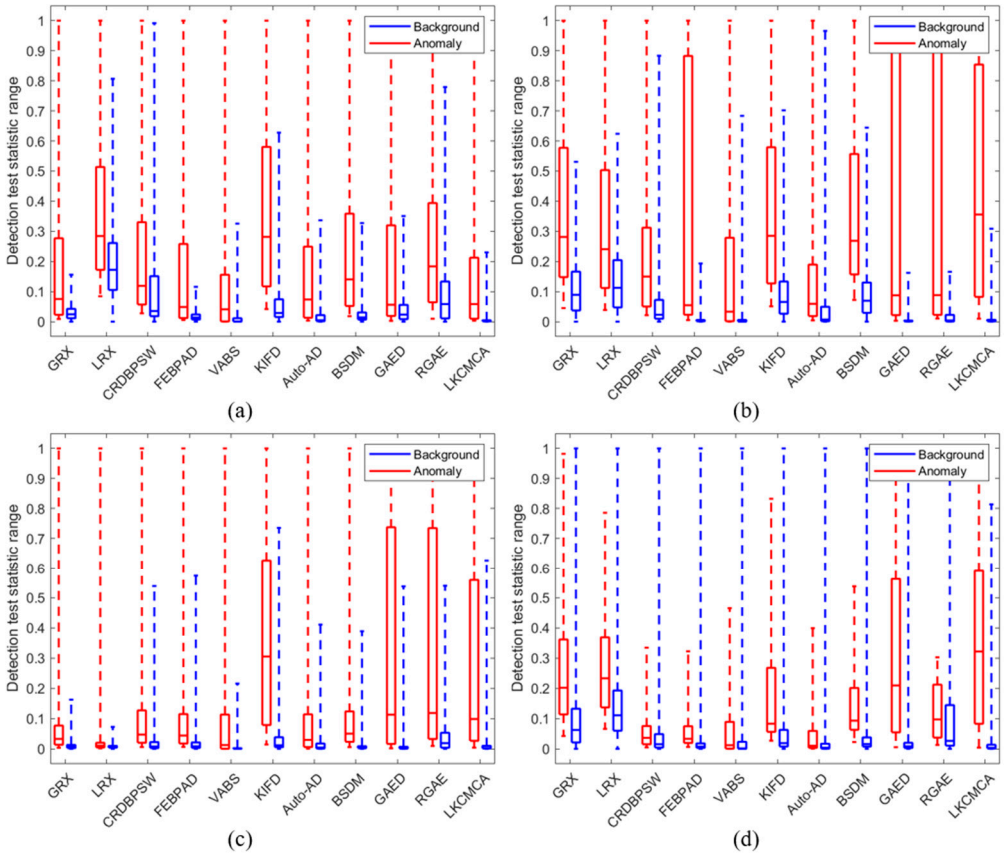


Figure 10. Separable boxplots of different algorithms on four datasets: (**a**) Data1, (**b**) Data2, (**c**) Data3, and (**d**) Data4.

Considering all these, from the HAD result maps, our proposed LKCMCA method demonstrates relatively superior visual results. In addition, LKCMCA has the highest average AUC of 0.9945, which is 0.008 higher than the average AUC of the second-ranked BSDM, as shown in Table 2. Meanwhile, by observing the HAD result maps and separable boxplots in combination, the false alarm rate of LKCMCA usually stays at a low level, which further ensures the balance between background suppression and anomaly detectability.

Table 2. AUC values of the 11 considered detectors on different datasets.

Data Set	Detectors and AUC Values										
	GRX	LRX	CRDBPSW	FEBPAD	VABS	KIFD	Auto-AD	BSDM	GAED	RGAE	LKCMCA
Data1	0.8490	0.8255	0.8600	0.8258	0.8696	0.9874	0.9426	0.9899	0.7927	0.8522	0.9906
Data2	0.9502	0.8499	0.9302	0.9950	0.9154	0.9621	0.8864	0.9833	0.9893	0.9555	0.9990
Data3	0.9657	0.7619	0.9528	0.9402	0.9025	0.9872	0.8761	0.9913	0.9798	0.9069	0.9901
Data4	0.9467	0.8903	0.7798	0.9554	0.7403	0.9358	0.7598	0.9816	0.9952	0.8053	0.9985
Average	0.9279	0.8319	0.8807	0.9291	0.8570	0.9681	0.8662	0.9865	0.9393	0.8800	0.9945

4. Discussion

This section presents an analysis of the effectiveness of the adopted channel attention mechanism and loss function, and comparison experiments all set the same parameters as outlined above. We conduct experiments on four datasets with the network that excludes the ECA module, the network that employs the L1 loss function, and the proposed LKCMCA network. Their AUC metrics are shown in Table 3. It can be seen that the AUC values are improved due to the inclusion of the ECA module. By comparing the HAD colored maps of the results obtained using the L1 loss function and our proposed loss

function in Figure 11, we can find that the anomalous responses of the detection results of LKCMCA are significantly enhanced. For example, the anomalous responses of the left targets in the Data1 dataset are significantly highlighted, and the anomalous targets that are barely visible originally become clearer after the use of the proposed loss function. The anomalous targets in the Data3 and Data4 datasets are also significantly highlighted. In addition, the comparison results of the HAD colored maps are not intuitive, since each of the two groups of experiments has a high or low target response in the Data2 dataset. Through the boxplots of the HAD results in Figure 12, we remain intuitively able to see that the red boxes of the HAD results using the proposed loss function are higher than those of the HAD results using the L1 loss function, and the distinction between anomalies and backgrounds is significantly improved. Although there is no significant improvement in the AUC value, the reconstruction of anomalous pixels is greatly suppressed. As can be seen from the results of the colored maps of Data3 and Data4, the proposed loss seems to have a slightly stronger anomalous response for some backgrounds and a slightly wider blue box in the boxplots compared to using the L1 loss. This is due to the fact that the proposed loss function reduces the loss weight of potential anomalous pixel locations, so that when reconstructing the sparsely distributed background, which is different in spectral characteristics from the surrounding background, the loss weight of this background is reduced accordingly, which suppresses its reconstruction effect and leads to higher anomaly responses in the corresponding detection results. This is still valuable because the use of the proposed loss function significantly restrains the reconstruction of anomalies, enhances the response values of the targets, and prevents the missed detection of some targets with weaker responses.

Table 3. AUC values of ablation study on different datasets.

Dataset	Detectors and AUC Values		
	Proposed Without ECA	**Proposed with L1 Loss Function**	**Proposed**
Data1	0.9882	0.9854	0.9906
Data2	0.9943	0.9986	0.9990
Data3	0.9751	0.9840	0.9901
Data4	0.9945	0.9985	0.9985

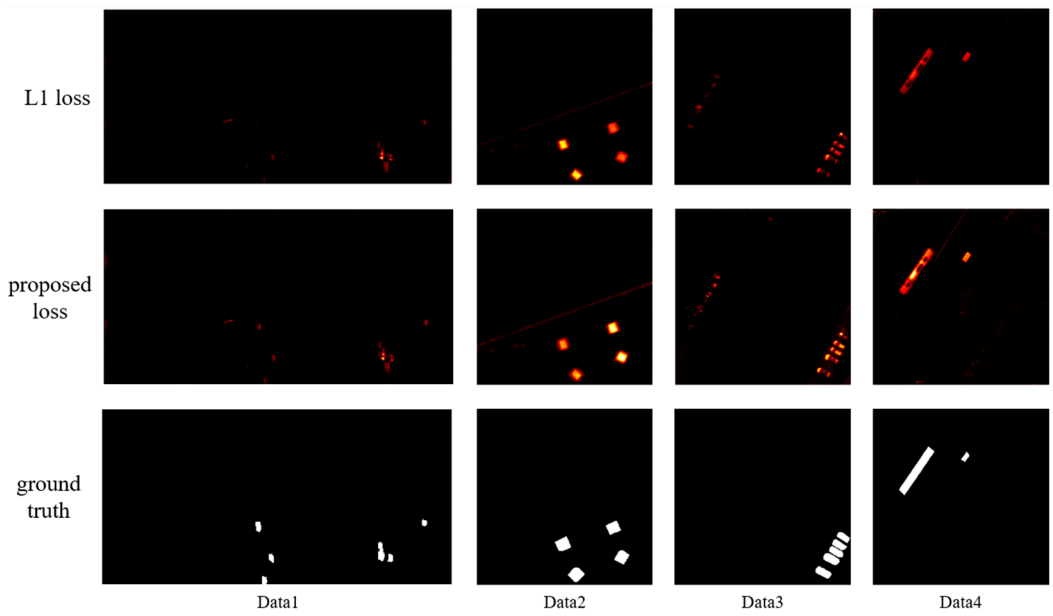


Figure 11. HAD colored maps obtained on the four datasets using the L1 loss function and the proposed loss function.

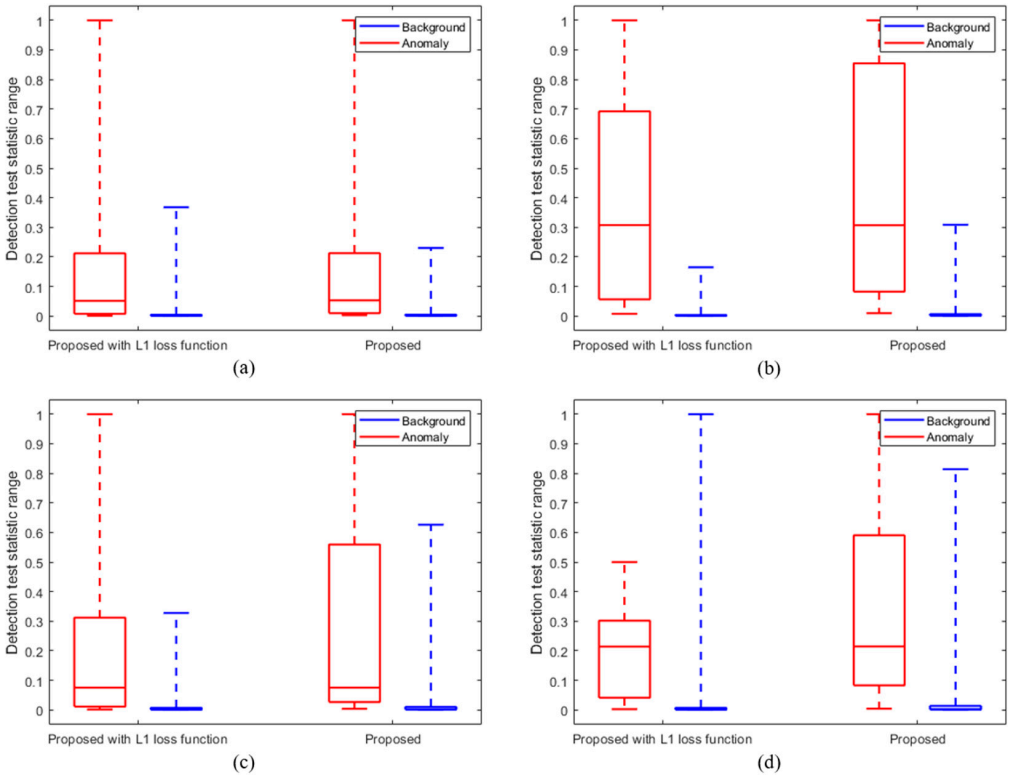


Figure 12. Separable boxplots of the HAD results on the four datasets using the L1 loss function and the proposed loss function: (**a**) Data1, (**b**) Data2, (**c**) Data3, and (**d**) Data4.

By analyzing the above experimental results, we find that the proposed LKCMCA method still has some limitations. In a complex scene containing anomalous targets and sparse background objects, the detection effect of our LKCMCA will be limited, and some of the sparse backgrounds will be detected as anomalies. Moreover, due to employing the large convolutional kernel, the network training speed is slower than some state-of-the-art methods. Therefore, in the future, we will design new frameworks to suppress sparsely distributed background objects, improve the detection accuracy in complex scenes, and adjust the network structure to accelerate the network training speed.

5. Conclusions

In this paper, we propose a new LKCMCA network for HAD, which integrates large-kernel central block masked convolution with channel attention. Firstly, the PD operation is applied to reduce the spatial correlation between anomalous targets and the background, effectively isolating the anomalous targets. Next, the large-kernel central block masked convolution is employed to reconstruct background information over a broader spatial scale, addressing the challenge of larger target scales inherent in HRHSI. The incorporation of inter-band information fusion further enhances the network's ability to suppress the reconstruction of anomalous pixels, significantly improving both background suppression and anomaly detection. Moreover, ablation experiments demonstrate that the proposed adaptive loss function effectively mitigates the reconstruction of anomalous pixels during network training. Comparison results against ten state-of-the-art methods across four datasets show that our proposed LKCMCA method consistently achieves superior performance, demonstrating robustness across varying scenarios and target scales.

Author Contributions: Conceptualization, H.Z. and D.W.; methodology, H.Z.; software, H.Z.; validation, H.Z., X.S. and D.W.; formal analysis, H.Z.; investigation, H.Z.; resources, H.Z.; data curation, H.Z.; writing—original draft preparation, H.Z. and D.W.; writing—review and editing, X.S.; visualiza-

tion, H.Z.; supervision, X.S. and Q.R.; project administration, Q.R., X.S. and H.S.; funding acquisition, Q.R., X.S. and H.S. All authors have read and agreed to the published version of the manuscript.

Funding: This research was funded by the National Natural Science Foundation of China (Grant No. 62301534), the Postdoctoral Fellowship Program (Grade B) of China Postdoctoral Science Foundation (Grant No. GZB20230777), China Postdoctoral Science Foundation (Grant No. 2024T170951), China Postdoctoral Science Foundation (Grant No. 2024M753306).

Data Availability Statement: The original contributions presented in this study are included in the article. Further inquiries can be directed to the corresponding author.

Conflicts of Interest: The authors declare no conflict of interest.

References

1. Goetz, A.F.; Vane, G.; Solomon, J.E.; Rock, B.N. Imaging Spectrometry for Earth Remote Sensing. *Science* **1985**, *228*, 1147–1153. [CrossRef] [PubMed]
2. Landgrebe, D. Hyperspectral Image Data Analysis. *IEEE Signal Process. Mag.* **2002**, *19*, 17–28. [CrossRef]
3. Zhang, L.; Zhang, Q.; Du, B.; Huang, X.; Tang, Y.Y.; Tao, D. Simultaneous Spectral-Spatial Feature Selection and Extraction for Hyperspectral Images. *IEEE Trans. Cybern.* **2018**, *48*, 16–28. [CrossRef] [PubMed]
4. Zhang, M.; Li, W.; Du, Q.; Gao, L.; Zhang, B. Feature Extraction for Classification of Hyperspectral and LiDAR Data Using Patch-to-Patch CNN. *IEEE Trans. Cybern.* **2020**, *50*, 100–111. [CrossRef] [PubMed]
5. Su, H.; Wu, Z.; Zhang, H.; Du, Q. Hyperspectral Anomaly Detection: A Survey. *IEEE Geosci. Remote Sens. Mag.* **2022**, *10*, 64–90. [CrossRef]
6. Wu, Z.; Sun, J.; Zhang, Y.; Zhu, Y.; Li, J.; Plaza, A.; Benediktsson, J.A.; Wei, Z. Scheduling-Guided Automatic Processing of Massive Hyperspectral Image Classification on Cloud Computing Architectures. *IEEE Trans. Cybern.* **2021**, *51*, 3588–3601. [CrossRef]
7. Zhang, Z.; Wang, D.; Sun, X.; Zhuang, L.; Liu, R.; Ni, L. Spatial Sampling and Grouping Information Entropy Strategy Based on Kernel Fuzzy C-Means Clustering Method for Hyperspectral Band Selection. *Remote Sens.* **2022**, *14*, 5058. [CrossRef]
8. Sun, X.; Qu, Y.; Gao, L.; Sun, X.; Qi, H.; Zhang, B.; Shen, T. Target Detection Through Tree-Structured Encoding for Hyperspectral Images. *IEEE Trans. Geosci. Remote Sens.* **2021**, *59*, 4233–4249. [CrossRef]
9. Gao, L.; Sun, X.; Sun, X.; Zhuang, L.; Du, Q.; Zhang, B. Hyperspectral Anomaly Detection Based on Chessboard Topology. *IEEE Trans. Geosci. Remote Sens.* **2023**, *61*, 5505016. [CrossRef]
10. Reed, I.S.; Yu, X. Adaptive Multiple-Band CFAR Detection of an Optical Pattern with Unknown Spectral Distribution. *IEEE Trans. Acoust. Speech Signal Process.* **1990**, *38*, 1760–1770. [CrossRef]
11. Molero, J.M.; Garzón, E.M.; García, I.; Plaza, A. Analysis and Optimizations of Global and Local Versions of the RX Algorithm for Anomaly Detection in Hyperspectral Data. *IEEE J. Sel. Top. Appl. Earth Observ. Remote Sens.* **2013**, *6*, 801–814. [CrossRef]
12. Kwon, H.; Nasrabadi, N.M. Kernel RX-Algorithm: A Nonlinear Anomaly Detector for Hyperspectral Imagery. *IEEE Trans. Geosci. Remote Sens.* **2005**, *43*, 388–397. [CrossRef]
13. Matteoli, S. Improved Estimation of Local Background Covariance Matrix for Anomaly Detection in Hyperspectral Images. *Opt. Eng.* **2010**, *49*, 046201. [CrossRef]
14. Liu, J.; Hou, Z.; Li, W.; Tao, R.; Orlando, D.; Li, H. Multipixel Anomaly Detection with Unknown Patterns for Hyperspectral Imagery. *IEEE Trans. Neural Netw. Learn. Syst.* **2022**, *33*, 5557–5567. [CrossRef]
15. Ren, L.; Ma, Z.; Bovolo, F.; Bruzzone, L. A Nonconvex Framework for Sparse Unmixing Incorporating the Group Structure of the Spectral Library. *IEEE Trans. Geosci. Remote Sens.* **2022**, *60*, 5506719. [CrossRef]
16. Zhuang, L.; Ng, M.K.; Liu, Y. Cross-Track Illumination Correction for Hyperspectral Pushbroom Sensor Images Using Low-Rank and Sparse Representations. *IEEE Trans. Geosci. Remote Sens.* **2023**, *61*, 5502117. [CrossRef]
17. Ma, X.; Zhang, X.; Tang, X.; Zhou, H.; Jiao, L. Hyperspectral Anomaly Detection Based on Low-Rank Representation with Data-Driven Projection and Dictionary Construction. *IEEE J. Sel. Top. Appl. Earth Observ. Remote Sens.* **2020**, *13*, 2226–2239. [CrossRef]
18. Wang, M.; Gao, L.; Ren, L.; Sun, X.; Chanussot, J. Hyperspectral Simultaneous Anomaly Detection and Denoising: Insights From Integrative Perspective. *IEEE J. Sel. Top. Appl. Earth Observ. Remote Sens.* **2024**, *17*, 13966–13980. [CrossRef]
19. Wang, M.; Hong, D.; Zhang, B.; Ren, L.; Yao, J.; Chanussot, J. Learning Double Subspace Representation for Joint Hyperspectral Anomaly Detection and Noise Removal. *IEEE Trans. Geosci. Remote Sens.* **2023**, *61*, 5507517. [CrossRef]
20. Li, W.; Du, Q. Collaborative Representation for Hyperspectral Anomaly Detection. *IEEE Trans. Geosci. Remote Sens.* **2015**, *53*, 1463–1474. [CrossRef]
21. Li, L.; Li, W.; Du, Q.; Tao, R. Low-Rank and Sparse Decomposition with Mixture of Gaussian for Hyperspectral Anomaly Detection. *IEEE Trans. Cybern.* **2021**, *51*, 4363–4372. [CrossRef] [PubMed]
22. Zhang, L.; Song, L.; Du, B.; Zhang, Y. Nonlocal Low-Rank Tensor Completion for Visual Data. *IEEE Trans. Cybern.* **2021**, *51*, 673–685. [CrossRef] [PubMed]
23. Zhang, Y.; Du, B.; Zhang, L.; Wang, S. A Low-Rank and Sparse Matrix Decomposition-Based Mahalanobis Distance Method for Hyperspectral Anomaly Detection. *IEEE Trans. Geosci. Remote Sens.* **2016**, *54*, 1376–1389. [CrossRef]

24. Zhuang, L.; Gao, L.; Zhang, B.; Fu, X.; Bioucas-Dias, J.M. Hyperspectral Image Denoising and Anomaly Detection Based on Low-Rank and Sparse Representations. *IEEE Trans. Geosci. Remote Sens.* **2022**, *60*, 5500117. [CrossRef]
25. Xu, Y.; Wu, Z.; Li, J.; Plaza, A.; Wei, Z. Anomaly Detection in Hyperspectral Images Based on Low-Rank and Sparse Representation. *IEEE Trans. Geosci. Remote Sens.* **2016**, *54*, 1990–2000. [CrossRef]
26. Qu, Y.; Wang, W.; Guo, R.; Ayhan, B.; Kwan, C.; Vance, S.; Qi, H. Hyperspectral Anomaly Detection Through Spectral Unmixing and Dictionary-Based Low-Rank Decomposition. *IEEE Trans. Geosci. Remote Sens.* **2018**, *56*, 4391–4405. [CrossRef]
27. Li, W.; Wu, G.; Du, Q. Transferred Deep Learning for Anomaly Detection in Hyperspectral Imagery. *IEEE Geosci. Remote Sens. Lett.* **2017**, *14*, 597–601. [CrossRef]
28. Rao, W.; Qu, Y.; Gao, L.; Sun, X.; Wu, Y.; Zhang, B. Transferable Network with Siamese Architecture for Anomaly Detection in Hyperspectral Images. *Int. J. Appl. Earth Obs. Geoinf.* **2022**, *106*, 102669. [CrossRef]
29. Bati, E.; Çalışkan, A.; Koz, A.; Alatan, A.A. Hyperspectral Anomaly Detection Method Based on Auto-Encoder. In Proceedings of the SPIE Remote Sensing, Toulouse, France, 21–24 September 2015. [CrossRef]
30. Wang, D.; Gao, L.; Qu, Y.; Sun, X.; Liao, W. Frequency-to-Spectrum Mapping GAN for Semisupervised Hyperspectral Anomaly Detection. *CAAI Trans. Intell. Technol.* **2023**, *8*, 1258–1273. [CrossRef]
31. Fan, G.; Ma, Y.; Mei, X.; Fan, F.; Huang, J.; Ma, J. Hyperspectral Anomaly Detection with Robust Graph Autoencoders. *IEEE Trans. Geosci. Remote Sens.* **2022**, *60*, 5511314. [CrossRef]
32. Wang, S.; Wang, X.; Zhang, L.; Zhong, Y. Auto-AD: Autonomous Hyperspectral Anomaly Detection Network Based on Fully Convolutional Autoencoder. *IEEE Trans. Geosci. Remote Sens.* **2022**, *60*, 5503314. [CrossRef]
33. Wang, X.; Wang, L.; Wang, Q. Local Spatial–Spectral Information-Integrated Semisupervised Two-Stream Network for Hyperspectral Anomaly Detection. *IEEE Trans. Geosci. Remote Sens.* **2022**, *60*, 5535515. [CrossRef]
34. Ma, J.; Xie, W.; Li, Y.; Fang, L. BSDM: Background Suppression Diffusion Model for Hyperspectral Anomaly Detection. *arXiv* **2023**, arXiv:2307.09861. [CrossRef]
35. Gao, L.; Wang, D.; Zhuang, L.; Sun, X.; Huang, M.; Plaza, A. BS3LNet: A New Blind-Spot Self-Supervised Learning Network for Hyperspectral Anomaly Detection. *IEEE Trans. Geosci. Remote Sens.* **2023**, *61*, 5504218. [CrossRef]
36. Wang, D.; Zhuang, L.; Gao, L.; Sun, X.; Huang, M.; Plaza, A.J. PDBSNet: Pixel-Shuffle Downsampling Blind-Spot Reconstruction Network for Hyperspectral Anomaly Detection. *IEEE Trans. Geosci. Remote Sens.* **2023**, *61*, 5511914. [CrossRef]
37. Wang, D.; Zhuang, L.; Gao, L.; Sun, X.; Huang, M.; Plaza, A. BockNet: Blind-Block Reconstruction Network with a Guard Window for Hyperspectral Anomaly Detection. *IEEE Trans. Geosci. Remote Sens.* **2023**, *61*, 5531916. [CrossRef]
38. Wang, D.; Zhuang, L.; Gao, L.; Sun, X.; Zhao, X.; Plaza, A. Sliding Dual-Window-Inspired Reconstruction Network for Hyperspectral Anomaly Detection. *IEEE Trans. Geosci. Remote Sens.* **2024**, *62*, 5504115. [CrossRef]
39. Wang, D.; Zhuang, L.; Gao, L.; Sun, X.; Zhao, X. Global Feature-Injected Blind-Spot Network for Hyperspectral Anomaly Detection. *IEEE Geosci. Remote Sens. Lett.* **2024**, *21*, 5509305. [CrossRef]
40. Cheng, X.; Zhang, M.; Lin, S.; Li, Y.; Wang, H. Deep Self-Representation Learning Framework for Hyperspectral Anomaly Detection. *IEEE Trans. Instrum. Meas.* **2024**, *73*, 5002016. [CrossRef]
41. Cheng, X.; Zhang, M.; Lin, S.; Zhou, K.; Zhao, S.; Wang, H. Two-Stream Isolation Forest Based on Deep Features for Hyperspectral Anomaly Detection. *IEEE Geosci. Remote Sens. Lett.* **2023**, *20*, 5504205. [CrossRef]
42. Cheng, X.; Huo, Y.; Lin, S.; Dong, Y.; Zhao, S.; Zhang, M.; Wang, H. Deep Feature Aggregation Network for Hyperspectral Anomaly Detection. *IEEE Trans. Instrum. Meas.* **2024**, *73*, 5033016. [CrossRef]
43. Zhong, Y.; Wang, X.; Xu, Y.; Wang, S.; Jia, T.; Hu, X.; Zhao, J.; Wei, L.; Zhang, L. Mini-UAV-Borne Hyperspectral Remote Sensing: From Observation and Processing to Applications. *IEEE Geosci. Remote Sens. Mag.* **2018**, *6*, 46–62. [CrossRef]
44. Zhong, Y.; Wang, X.; Wang, S.; Zhang, L. Advances in Spaceborne Hyperspectral Remote Sensing in China. *Geo. Spat. Inf. Sci.* **2021**, *24*, 95–120. [CrossRef]
45. Li, Y.; Xu, J.; Xia, R.; Wang, X.; Xie, W. A Two-Stage Framework of Target Detection in High-Resolution Hyperspectral Images. *SIViP* **2019**, *13*, 1339–1346. [CrossRef]
46. Shibi, S.; Rajagopal, G. Target Object Detection Using Chicken Social-Based Deep Belief Network with Hyperspectral Imagery. *IET Image Process.* **2020**, *14*, 3781–3790. [CrossRef]
47. Wang, Z.; Liu, J.; Li, G.; Han, H. Blind2Unblind: Self-Supervised Image Denoising with Visible Blind Spots. In Proceedings of the 2022 IEEE/CVF Conference on Computer Vision and Pattern Recognition (CVPR), New Orleans, LA, USA, 18–24 June 2022; IEEE: New Orleans, LA, USA, 2022; pp. 2017–2026.
48. Shi, W.; Caballero, J.; Huszar, F.; Totz, J.; Aitken, A.P.; Bishop, R.; Rueckert, D.; Wang, Z. Real-Time Single Image and Video Super-Resolution Using an Efficient Sub-Pixel Convolutional Neural Network. In Proceedings of the 2016 IEEE Conference on Computer Vision and Pattern Recognition (CVPR), Las Vegas, NV, USA, 27–30 June 2016; pp. 1874–1883. [CrossRef]
49. Wang, Q.; Wu, B.; Zhu, P.; Li, P.; Zuo, W.; Hu, Q. ECA-Net: Efficient Channel Attention for Deep Convolutional Neural Networks. In Proceedings of the 2020 IEEE/CVF Conference on Computer Vision and Pattern Recognition (CVPR), Seattle, WA, USA, 13–19 June 2020; pp. 11531–11539.
50. Rangnekar, A.; Mokashi, N.; Ientilucci, E.J.; Kanan, C.; Hoffman, M.J. AeroRIT: A New Scene for Hyperspectral Image Analysis. *IEEE Trans. Geosci. Remote Sens.* **2020**, *58*, 8116–8124. [CrossRef]
51. Chang, C.-I. An Effective Evaluation Tool for Hyperspectral Target Detection: 3D Receiver Operating Characteristic Curve Analysis. *IEEE Trans. Geosci. Remote Sens.* **2021**, *59*, 5131–5153. [CrossRef]

52. Hou, Z.; Li, W.; Tao, R.; Ma, P.; Shi, W. Collaborative Representation with Background Purification and Saliency Weight for Hyperspectral Anomaly Detection. *Sci. China Inf. Sci.* **2022**, *65*, 112305. [CrossRef]
53. Hou, Z.; Li, W.; Li, L.; Tao, R.; Du, Q. Hyperspectral Change Detection Based on Multiple Morphological Profiles. *IEEE Trans. Geosci. Remote Sens.* **2022**, *60*, 5507312. [CrossRef]
54. Hou, Z.; Li, W.; Tao, R.; Du, Q. Three-Order Tucker Decomposition and Reconstruction Detector for Unsupervised Hyperspectral Change Detection. *IEEE J. Sel. Top. Appl. Earth Observ. Remote Sens.* **2021**, *14*, 6194–6205. [CrossRef]

Disclaimer/Publisher's Note: The statements, opinions and data contained in all publications are solely those of the individual author(s) and contributor(s) and not of MDPI and/or the editor(s). MDPI and/or the editor(s) disclaim responsibility for any injury to people or property resulting from any ideas, methods, instructions or products referred to in the content.